energies

MDPI

Article

Pressure Exchanger for Energy Recovery in a Trans-Critical CO_2 Refrigeration System

Ahmed Elatar *, Brian Fricke, Vishaldeep Sharma and Kashif Nawaz

Oak Ridge National Laboratory, Oak Ridge, TN 37830, USA; frickeba@ornl.gov (B.F.); sharmav@ornl.gov (V.S.); nawazk@ornl.gov (K.N.)

* Correspondence: elataraf@ornl.gov

Abstract: Trans-critical CO_2 vapor compression (VC) refrigeration cycles require a high compression ratio, which is associated with high expansion losses. To recover these expansion losses, a pressure exchange process between the low- and high-pressure sides of the VC cycle is proposed and examined in this study. The proposed pressure exchange system is an open type constant volume process where the high- and low-pressure flows mix inside the system. This prototype is inspired by the pressure exchangers used in reverse-osmosis (RO) desalination systems. In this system, a 2D model was generated and modeled using the computational fluid dynamics (CFD) technique. The numerical model ignored any losses due to leakage or hydraulic friction and the process is considered adiabatic. For the modeling, it was assumed that the inlet conditions for the two pressure exchanger flows are similar to the flow conditions at the evaporator and gas cooler outlets in a VC cycle. Two parameters are examined to test the validity of the system and understand their effect on the performance, including the inlet flow rate represented by the inlet velocity and the process time represented by the speed of rotation. A total of nine cases were simulated and analyzed in this study.

Keywords: pressure exchanger; trans-critical CO_2 refrigeration cycle; energy recovery

Citation: Elatar, A.; Fricke, B.; Sharma, V.; Nawaz, K. Pressure Exchanger for Energy Recovery in a Trans-Critical CO_2 Refrigeration System. *Energies* **2021**, *14*, 1754. https://doi.org/10.3390/en14061754

Academic Editor: Fabio Polonara

Received: 4 February 2021
Accepted: 17 March 2021
Published: 22 March 2021

1. Introduction

Global warming and its detrimental effects on the planet have forced action among scientists, politicians, and the general public. Among the efforts to tackle this problem includes replacing high global warming potential (GWP) refrigerants with lower GWP refrigerants in vapor compression systems used in the applications of heating, ventilation and air conditioning, and refrigeration (HVAC-R). One of the promising low GWP candidate refrigerants is carbon dioxide (CO_2). Since CO_2 is nontoxic and nonflammable, it is considered to be a very good refrigerant choice for commercial refrigeration applications in supermarkets and warehouses [1,2]. The major challenges associated with using CO_2 as a refrigerant are its low critical temperature and high operating pressure. This leads to lower system performance at warmer ambient conditions and higher expansion losses, respectively. However, researchers are continuously improving refrigeration technology to overcome the lower system performance in warm and hot climates [3]. Figure 1a shows a typical CO_2 vapor compression cycle. Heat is absorbed by the refrigerant in the evaporator to provide cooling. The refrigerant from the medium-temperature compressors enters a gas cooler/condenser and rejects heat to the surroundings. The refrigerant exiting the gas cooler/condenser is expanded through a high-pressure expansion valve before entering a flash tank for phase separation. The liquid refrigerant is split into two streams and further expands to the saturation pressure corresponding to the medium-temperature and low-temperature loads, respectively. After absorbing heat from the low-temperature loads, the low-temperature refrigerant is superheated by passing through the flash tank before being compressed in the low-temperature compressors. The low-temperature compression outlet mixes with medium-temperature refrigerant before both streams are compressed in the medium-temperature compressors.

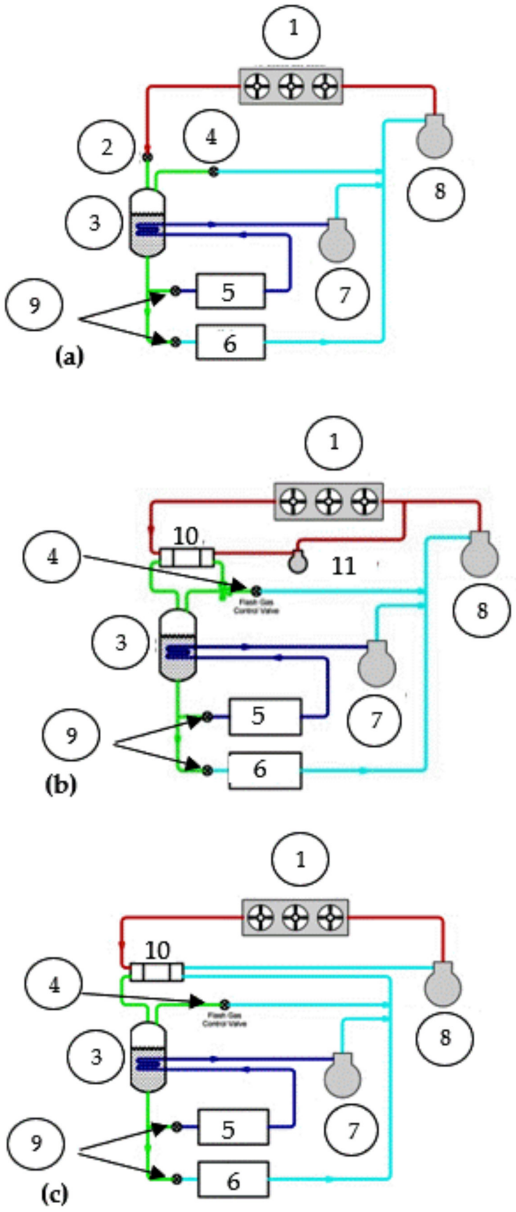

#	Part
1	Air-cooled Gas Cooler
2	High Pressure Expansion Valve
3	Flash Tank
4	Flash Tank Control Valve
5	Low Temperature Load
6	Medium Temperature Load
7	Low Temperature Compressor
8	Medium Temperature Compressor
9	Expansion Valves
10	Pressure Exchanger
11	Booster Compressor

Figure 1. Trans-critical CO_2 booster refrigeration system configurations: (**a**) Basic cycle without pressure exchanger, (**b**) Cycle with pressure exchanger on flash gas bypass, and (**c**) Cycle with pressure exchanger on medium-temperature compressor suction.

The irreversibility associated with compression and expansion processes represents a significant portion of the total irreversibility in vapor compression refrigeration cycles. Throttling and compression losses can be reduced by taking advantage of the flow work which is otherwise lost when refrigerant is expanded from high pressure to low pressure. This is particularly attractive for CO_2 refrigeration systems since a high mean pressure exists and a significant amount of work can be produced in the liquid phase. One way of improving the thermodynamic cycle performance is by utilizing the high-pressure CO_2 leaving the gas cooler (condenser for typical refrigerants) to exchange kinetic energy with the low-pressure refrigerant before entering the compressor. One way to accomplish this is by using an ejector expansion device. In an ejector, the high-pressure stream exiting the gas cooler expands through a nozzle, partially compressing the vapor refrigerant exiting the evaporator. The cycle efficiency is increased because the compressor operates at a

reduced pressure ratio as compared to a cycle without an ejector. Analysis shows that the simple CO_2 refrigeration system cycle efficiency may increase by up to 20% with an ejector expansion device [4]. However, system control is challenging since a combination of liquid and vapor expanders is required.

Ejectors have been studied for energy recovery by applying experimental and numerical tools. Nakagawa et al. [5] experimentally studied a CO_2 refrigeration cycle with an ejector for performance enhancement. Further, Nakagawa et al. [6] examined adding a heat exchanger to the cycle for even better enhancement. Elbel and Hrnjak [7] experimentally evaluated an ejector prototype in a trans-critical CO_2 refrigeration cycle. Also, ejectors have been modeled numerically to assess their operation by Bartosiewicz et al. [8] and Banasiak and Hafner [9]. Besagni et al. [10] presented a comprehensive review of ejector technology in refrigeration cycles. A CO_2 refrigeration cycle was optimized using a controlled ejector with a variable nozzle throat area by He et al. [11]. Research on ejectors continues to find the optimum design. Carrillo et al. [12] optimized ejector geometry using multi-objective optimization and a surrogate CFD model. Carrillo et al. [13] conducted a thermodynamic analysis to find the optimum operating conditions for CO_2 refrigeration units in warm climates with and without an ejector.

Another technology that takes advantage of exchanging energy in the cycle can be found in the reverse osmosis (RO) water desalination industry. A pressure exchanger can be used in RO systems to transfer energy to the low-pressure flow (seawater) from the high-pressure flow (brine). A pressure exchanger (PX) has been investigated numerically and experimentally [14–17]. The PX consists of two stationary end plates and a rotor in-between. The rotor is a cylindrical structure with an array of channels arranged around the center axis. The rotor spins between the two stationary end plates, each of which contains ports for controlling fluid flow into and out of the rotor channels. During rotation, the channel ends are periodically exposed to differing port pressures, initiating compression and expansion within the rotor channels. This results in raising the secondary flow pressure and decreasing the primary flow pressure.

An attractive application of the pressure exchanger is to increase the efficiency of trans-critical CO_2 refrigeration cycles. There are two possible configurations for the modified cycle. One configuration is to pass the high-pressure refrigerant stream from the gas cooler into the pressure exchanger in order to increase the pressure of the flash gas exiting the flash tank (Figure 1b). A significant flow of flash gas exists, particularly when the ambient temperature is high, and this flash gas does not produce any useful refrigerating effect. Rather than using the medium-temperature compressors to compress this flash gas, a pressure exchanger can be used to increase the pressure of the flash gas stream, thereby reducing the power consumption of the medium-temperature compressors. In the other configuration, the medium-temperature suction flow passes through the pressure exchanger prior to entering the medium-temperature compressors (Figure 1c). The refrigerant exiting the gas cooler is the high-pressure flow responsible for increasing the medium-temperature flow pressure before entering the compressor. This will result in less compressor energy consumption. In both configurations, expansion valves are used to achieve the desired refrigerant state before entering the evaporator coil.

This paper is intended to present a new concept, the pressure exchanger (PX), for energy exchange within the trans-critical CO_2 refrigeration cycle. The PX is modeled and simulated to characterize its performance, using computational fluid dynamics (CFD). Figure 2 shows a simplified model of the PX, where the boundary conditions are adapted from the trans-critical CO_2 VC system. A thermodynamic analysis is performed based on the CFD simulation predictions.

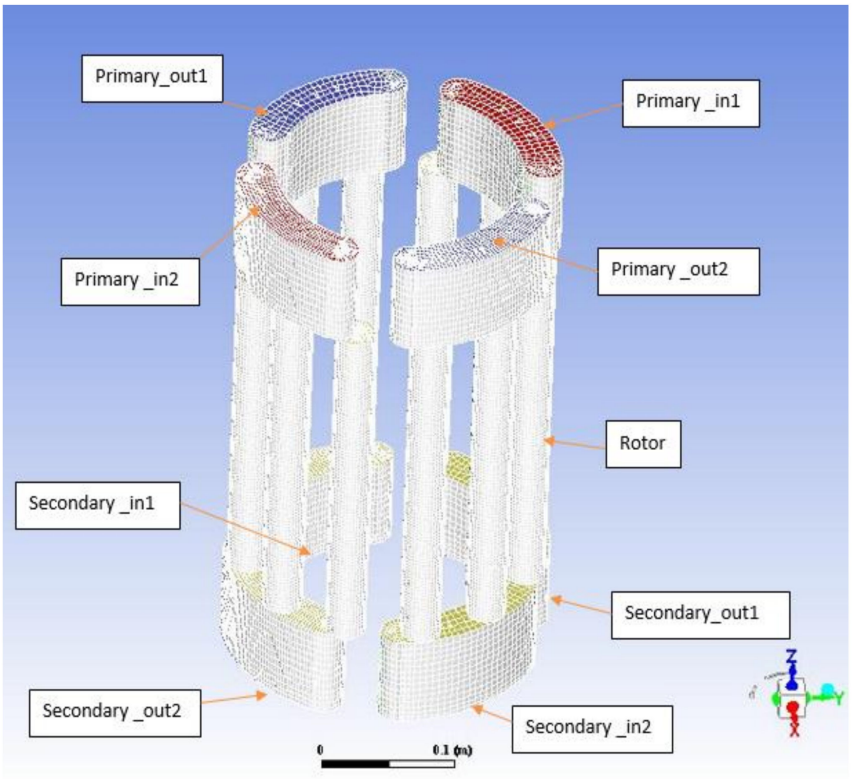

Figure 2. 3D CAD model of PX and generated mesh.

2. Materials and Methods

2.1. 3D Pressure Exchanger Model

A 3D computer aided design (CAD) model for the pressure exchanger was developed, as shown in Figure 2. The model is inspired by the PX design found in RO systems. The model components and boundary conditions are illustrated in Figure 2. On one end of the PX, there are two sets of primary (high pressure) flow inlets and outlets, while on the other end of the PX, there are two sets of secondary (low pressure) flow inlets and outlets. The rotor of the PX was modeled with 9 channels. The PX model has the following dimensions:

Rotor channel length = 0.19 m
Rotor channel diameter = 0.02 m
Rotor outside diameter = 0.18 m
Inlet/outlet port depth = 0.05 m

The PX model is designed to execute two compression strokes in a single rotation. ANSYS Workbench was used to create the model and generate the mesh. The mesh was refined at the inlets and outlets, and a total of 316×10^3 cells were used based on a grid dependency analysis. The transient pressure-based coupled algorithm CFD model was selected to simulate the system. The continuity and momentum equations are solved in a coupled manner. The spatial discretization was performed by using a second order upwind scheme while the transient formulation was performed by using a first order implicit scheme.

The governing equations used to model the flow are as follows.

Continuity equation:

$$\frac{\partial \rho}{\partial t} + \nabla \cdot \left(\rho \vec{v}\right) = S_m \quad (1)$$

where ρ is the fluid density, t is time, v is the fluid velocity, and S_m is the mass source term.

Momentum equation:

$$\frac{\partial}{\partial t}\left(\rho\vec{v}\right) + \nabla \cdot \left(\rho\vec{v}\vec{v}\right) = -\nabla p + \nabla \cdot \left(\bar{\bar{\tau}}\right) + \rho\vec{g} + \vec{F} \quad (2)$$

where p is the static pressure, $\bar{\bar{\tau}}$ is the stress tensor, $\rho\vec{g}$ and $\vec{F}$ are the gravity and body forces, respectively.

Energy equation:

$$\frac{\partial}{\partial t}(\rho E) + \nabla \cdot \left(\vec{v}\,(\rho E + p)\right) = \nabla \cdot \left\{k_{eff}\,\nabla T - \sum_j h_j \vec{J}_j + \left(\bar{\bar{\tau}}_{eff} \cdot \vec{v}\right)\right\} + S_h \quad (3)$$

where E is the total volume energy density, k_{eff} is the effective conductivity which includes turbulent conductivity defined by the turbulence model, h_j is the enthalpy, $\vec{J}_j$ is the diffusion flux of species j, and S_h is the energy source term.

Turbulence modeling was considered in the simulation and modeled by the Realizable k-ε turbulence model. The model is described by the following two transport equations:

Turbulence kinetic energy:

$$\frac{\partial}{\partial t}(\rho k) + \frac{\partial}{\partial x_j}(\rho k u_j) = \frac{\partial}{\partial x_j}\left[\left(\mu + \frac{\mu_t}{\sigma_k}\right)\frac{\partial k}{\partial x_j}\right] + G_k + G_b - \rho\varepsilon - Y_M + S_k \quad (4)$$

where k is the turbulence kinetic energy, μ is the dynamic viscosity, μ_t is the eddy viscosity, σ_k is the turbulent Prandtl number, G_k is the generation of turbulence kinetic energy due to the mean velocity gradients, G_b is the generation of turbulence kinetic energy due to buoyancy, S_k is a source term, and Y_M is the contribution of the fluctuating dilatation in compressible turbulence to the overall dissipation rate.

Turbulent dissipation rate

$$\frac{\partial}{\partial t}(\rho\varepsilon) + \frac{\partial}{\partial x_j}(\rho\varepsilon u_j) = \frac{\partial}{\partial x_j}\left[\left(\mu + \frac{u_t}{\sigma_\varepsilon}\right)\frac{\partial \varepsilon}{\partial x_j}\right] + \rho C_1 S_\varepsilon - \rho C_2 \frac{\varepsilon^2}{k + \sqrt{v\varepsilon}} + C_{1\varepsilon}\frac{\varepsilon}{k} C_{3\varepsilon} G_b + S_\varepsilon \quad (5)$$

where ε is the turbulent dissipation rate, σ_ε is the turbulent Prandtl number, S_ε is a source term, C_1 is max of [0.43, $\eta/\eta + 5$] where $\eta = S\,k/\varepsilon$, C_2, $C_1\varepsilon$ and $C_3\varepsilon$ are constants.

The turbulent kinetic energy equation is a representation of the turbulent kinetic energy generated due to the velocity gradient (G_k) and buoyancy (G_b). This model is different from the standard k-ε turbulence model in two ways. The turbulent viscosity is variable and secondly, the turbulent dissipation rate equation is derived from an exact equation of the mean-square vorticity fluctuation. This model yields a better prediction of more complex flows. For further details about this turbulence model, refer to the ANSYS Fluent 17.2 user's manual.

Carbon dioxide is modeled as a real gas, and the refrigerant properties were calculated by REFPROP 9.1 [18]. In the current study, modeling of the rotor rotational driving force is not considered for simplicity and the rotor rotational motion is set at different speeds.

2.2. Numerical Validation

Due to a lack of available experimental data for pressure exchangers operating with CO_2, the CFD model was validated against published experimental data by Xu et al. [19] for pressure exchanger testing to recover energy in a water desalination system. The high-pressure flow is a brine with a 6% mass fraction of sodium chloride, and the low-pressure flow is seawater with 3% by the mass fraction of sodium chloride. Velocity inlet and pressure outlets were selected for the numerical model boundary conditions. A total of seven modeling cases were considered for comparison between the two available sets of experimental data. The inlet volume flow rate and rotor rotational speed are the two

varying parameters considered. Dimensionless inflow length (L) and mixing are calculated from the numerical results and compared against the experimental data. Dimensionless inflow length is defined as follows:

$$L = (\varnothing \times Q(a + \beta))/120\pi \times m \times s \times n)/H \quad (6)$$

where $\varnothing$ is a correction factor (considered as 0.8), Q is the flow rate (m^3/hr), α is the central port angle, β is the central angle of one rotor channel, n is the rotor speed (rpm), s is the area of one rotor channel (m^2), m is the whole minimum number of the rotor channels covered by one port (n = 3), and H is the rotor length (m). The mixing is defined as:

$$Mixing = \frac{S_{s\_out} - S_{s\_in}}{S_{b\_in} - S_{s\_in}} \quad (7)$$

where S is the salinity level, subscript b refers to brine, and subscript s refers to sea water. Mixing is the term that quantifies the amount of mixing which occurs between the brine and seawater inside the pressure exchanger. Figure 3 shows the relation between L and the percent of Mixing. The results show a good agreement between the numerical and experimental data. The average deviation between the numerical and experimental results is about 10%. The CFD model overpredicted mixing compared to the experimental data.

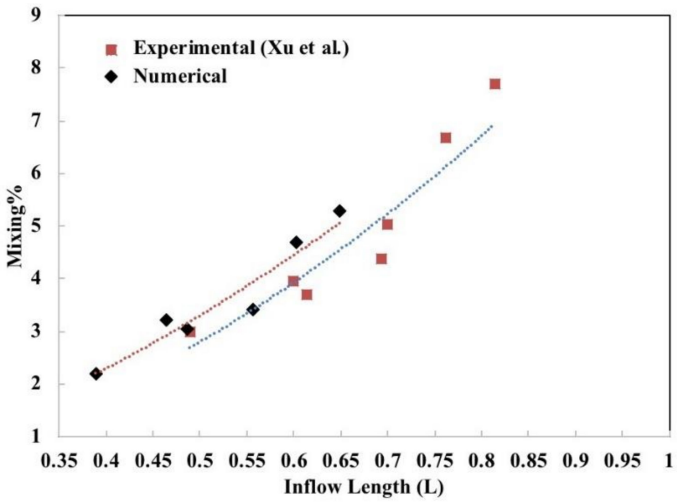

Figure 3. Percent mixing as a function of the dimensionless inflow length for the experimental and numerical results.

This discrepancy can be justified by the fact of ignoring leakage losses in the CFD model, whereas in the experimental test, the pressure exchanger suffers losses due to leakage between the rotor and the inlet and outlet ports.

2.3. 2D Pressure Exchanger Model

After validating the numerical modeling methodology with the available published data, several simulation trials were executed for the 3D PX model using carbon dioxide as real gas flow. It was found that the simulation did not converge with the grid size and time step applied in the validation process. The grid was further refined (total of 1.8 million cells), and the time step was reduced to 10^{-4} s. Due to these modifications, the simulation time increased significantly. Given the resource limitation at hand, the 3D model was simplified into a 2D model to reduce the simulation time. The numerical model parameters are kept identical to the validated model. The simplified model represents a single compression chamber, and the process was assumed symmetric in the third space coordinate.

The schematic in Figure 4 shows the 2D pressure exchanger model and illustrates the processes of the compression stroke. The 2D model consists of two insulated sidewalls, and the system is assumed adiabatic. The bottom side of the system is the inlet port while the top end is the discharge port. Both low- and high-pressure flows enter the chamber through the same inlet. The simplified system is considered as an open type due to mixing inside the chamber. Hereinafter, the high-pressure flow is referred to as the primary flow while the low-pressure flow is referred to as the secondary flow.

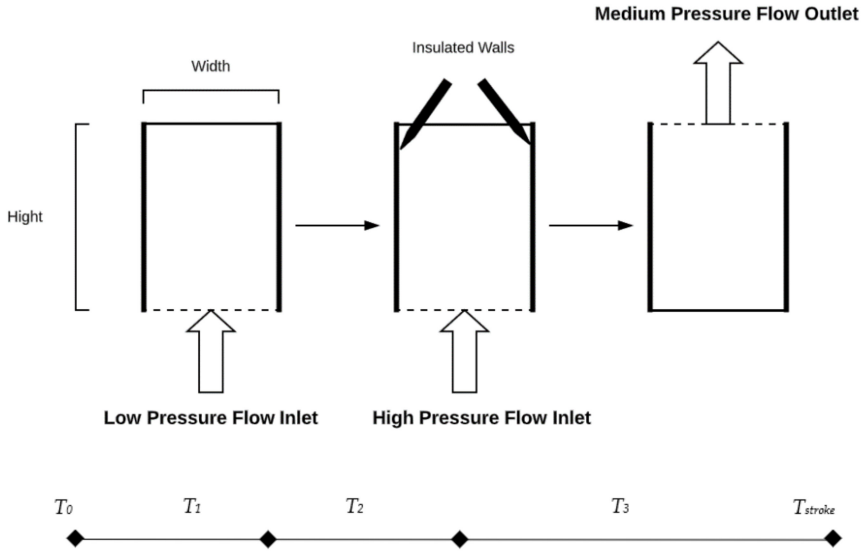

Figure 4. Schematic of the 2D model.

The compression stroke consists of three processes. The first process is filling the chamber with the secondary flow. The second process is compression. In this process, the primary flow enters the chamber and mixes with the secondary flow and results in a medium pressure mixture ($P_{low} < P_{mixture} < P_{high}$). In these two processes, the outlet port stays closed to allow for charging and compression. The third and final process of the compression stroke is the discharge process. During this process, the inlet port closes entirely while the outlet port opens to discharge the gas mixture. Table 1 shows the three processes in order and the associated boundary conditions. The time duration of the filling and compression processes are the same ($T_1 = T_2$) while the time duration of the discharge process is twice that of either the filling or compression process ($T_3 = T_1 + T_2$). The compression stroke time is calculated as follows:

$$T_{stroke} = \frac{1}{N/60} = T_1 + T_2 + T_3 \quad (8)$$

Table 1. Boundary Conditions of the compression stroke.

Process Number	Process	Inlet	Outlet	Boundary Condition	Temperature (K)	Duration (Seconds)
1	Filling	Open	Close	Velocity Inlet	290	$\frac{60}{4N}$
2	Compression	Open	Close	Velocity Inlet	290	$\frac{60}{4N}$
3	Discharge	Close	Open	Pressure Outlet	290 *	$\frac{60}{2N}$

* Backflow properties.

Generally, the three processes are timed according to the system speed of rotation and the number of compression strokes per revolution. This simplified model can be simulated for any speed of rotation and number of strokes per revolution. In the current study, a single stroke per revolution is considered, and three rotational speeds are simulated (N = 1500, 3000, and 4500 RPM).

The 2D CFD simulations were performed to investigate the effects of two parameters: rotational speed (N) and inlet velocity (V). Three rotational speeds and three inlet velocities were selected for simulation and are listed in Table 2. Steady-state conditions are assumed for the CFD model. Mass conservation was observed for the whole compression stroke. In other words, the inlet and outlet masses into the system were equal to eliminate any accumulation inside the channel and to guarantee the steadiness of the process.

Table 2. Operating conditions.

Case Number	Rotational Speed (RPM)	Inlet Velocity (m/s)
Case 1	1500	0.5
Case 2		1
Case 3		2
Case 4	3000	0.5
Case 5		1
Case 6		2
Case 7	4500	0.5
Case 8		1
Case 9		2

3. Results

The nine simulated cases are presented in this section. The influence of the pressure and temperature boundary conditions are not considered in this study, while the focus is on understanding the system behavior under different rotational speed and flow rate conditions. The following results are the representation of the area average properties inside the system for each investigated case.

Figure 5a–c shows the total pressure variation during the cycle. One can observe that the profile trends are similar for the nine cases. The pressure gradually increases during the filling process, which lasts for one-fourth of the whole cycle. The average pressure at the end of this process shows a minimal difference among the cases. As one expects, the longer the charging process time, the higher the process final pressure. During the compression process, the primary flow is charged into the system and rapidly increases the internal pressure until reaching a maximum value at the end of the compression process. This second state represents the mixed flow final pressure.

During the discharge process, the internal pressure rapidly decreases with time as the flow is being discharged from the system. The three figures clearly show the effect of the inlet mass flow rate on the compression. That is, as the flow rate increases at a given rotational speed, the internal pressure increases. The profiles seen in the figures indicates a monotonic increase of the internal pressure with inlet velocity at a given rotation speed. This behavior is consistent for all rotation speeds.

On the other hand, the rotational speed (i.e., the process time) shows a distinct effect on the internal system pressure, as seen in Figure 5a–c. As the rotational speed increases, the compression process shows a decrease in the compression rate. This is due to the shorter stroke time. At a given flow rate, Figure 5a–c show that the highest pressure occurs during the slowest rotational speed of 1500 RPM. A monotonic decrease of maximum pressure is observed with the rotational speed increase. The maximum internal pressure at the end of the compression process ranges from 20 MPa for Case 3 to 3.5 MPa for Case 8. The results indicate that the rotational speed can control the outlet pressure, which is necessary for the design of any trans-critical CO_2 cycle and the broader applicability of the system.

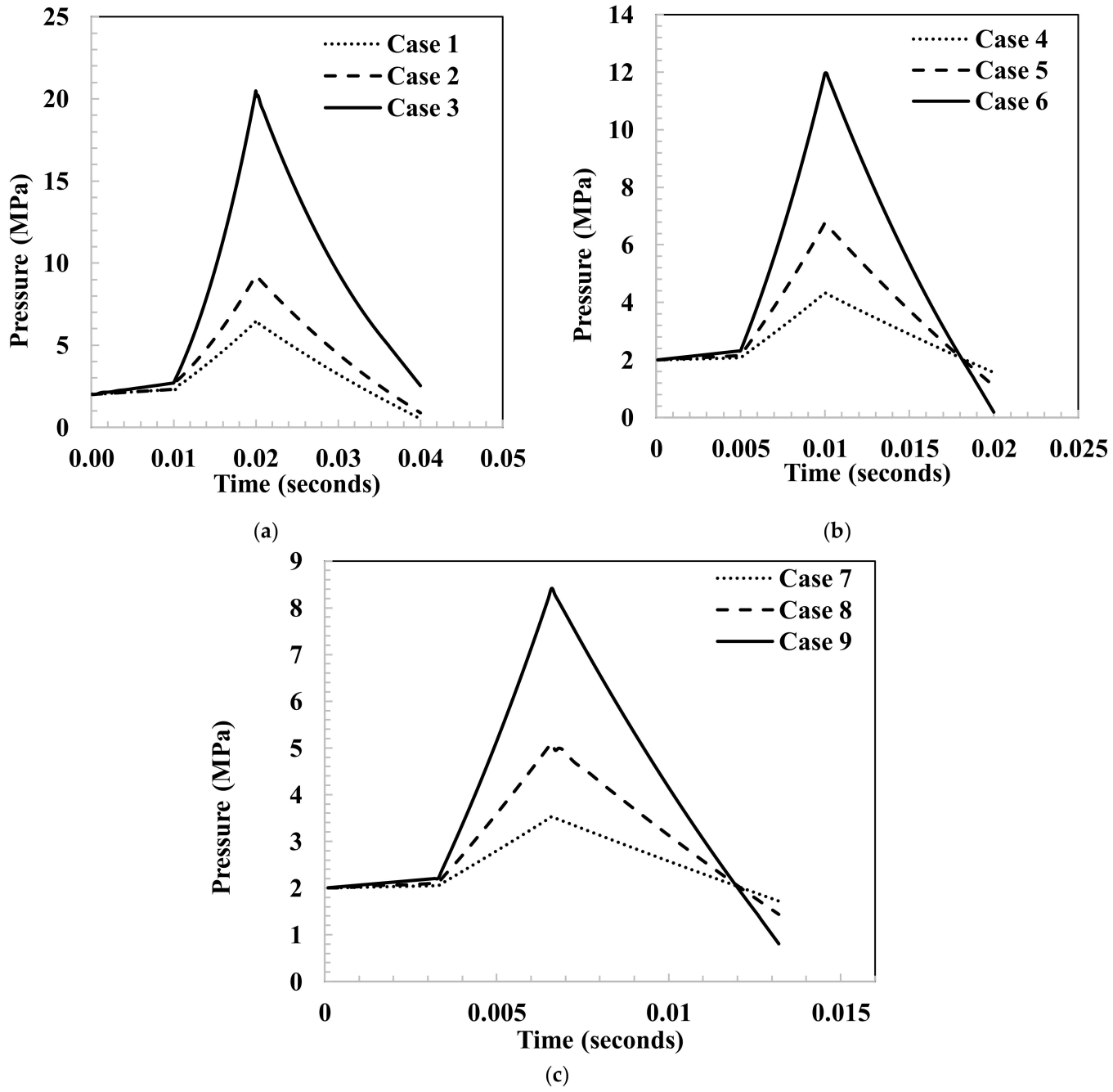

Figure 5. Average Internal Pressure at (**a**) 1500 RPM, (**b**) 3000 RPM and (**c**) 4500 RPM.

Although the inlet velocity increase has a similar influence on system pressure for most of the stroke time, an interesting observation can be seen close to the end of the compression stroke for the higher two rotational speed as seen in Figure 5b,c. That is, the system pressure reaches an inflection point where the relationship between inlet velocity and system pressure is inverse. This means that the highest system pressure, which occurs at the maximum inlet velocity (Cases 6 and 9), drops to become the lowest system pressure. Moreover, the second-highest system pressure drops to become the second-lowest system pressure. This change takes place at an instant around 75% of the discharge process time. This behavior can be explained and justified. The generated system pressure is enhanced proportionally with the increase of inlet velocity (flow rate), which creates a higher-pressure difference between the system and the conditions in the surrounding. Thus, the discharge

flow rate will be higher, which means a greater system pressure drop will occur as a result. This behavior continues from the discharge process onset until the end of the process. This is observed for all rotational speeds considered in the study. However, this inflection is not seen at the lowest system speed of 1500 RPM, as seen in Figure 5a. This is due to the fact that the maximum system pressure is achieved at that rotational speed and the system rate of pressure drop during the discharging process is not large enough to lower the system pressure relatively, as noticed in Figure 5b,c.

The average internal temperature for each process of the cycle are shown in Figure 6a–c. The profiles follow a similar trend as observed previously for the pressure profiles. The internal average temperature shows a slight increase during the filling process, followed by a sharp increase during the compression process. The temperature increase during the compression process decreases gradually at the onset of the discharge process. This monotonic behavior is observed for both the internal pressure and the temperature values. That is, the rate of increase of internal temperature is proportional to the increase in inlet velocity, while the increase in rotational speed has an inverse effect on the rate of increase of internal temperature. The highest increase in system temperature takes place at the end of the compression process and is approximately 29 K for Case 3, while the lowest increase is around 2 K for Case 7. The pressure and temperature profiles clearly predict the thermodynamic behavior of the cycle.

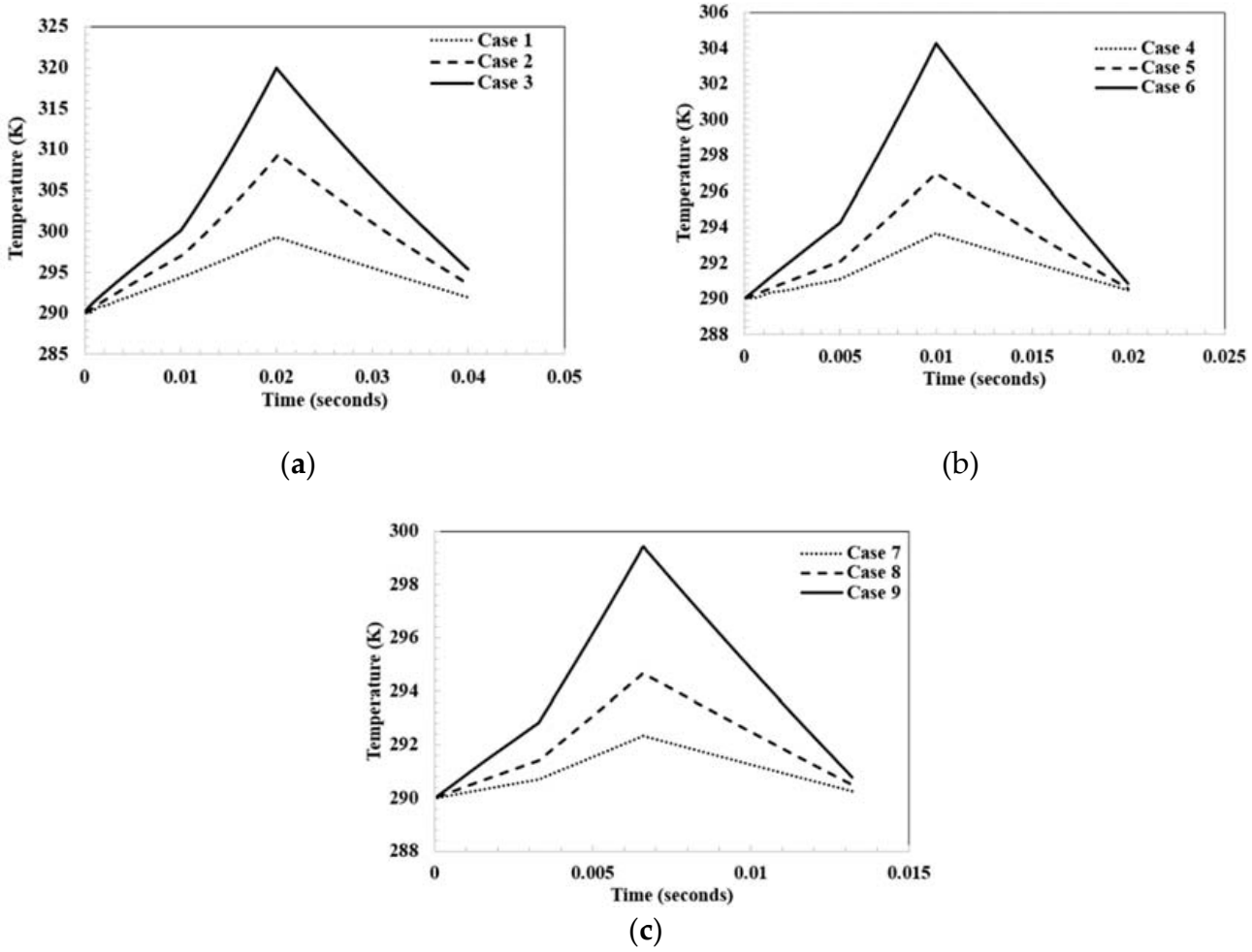

Figure 6. Average Internal Temperature for system rotational speed of (**a**) 1500 RPM, (**b**) 3000 RPM and (**c**) 4500 RPM.

At the end of the discharge process, the internal temperature shows a slight increase compared to the initial temperature. This increase is more noticeable at longer cycle time (lower rotational speed) and higher inlet velocity (Figure 6a). This observation highlights the importance of maintaining steady internal temperature during the operation of a pressure exchanger system.

Table 3 shows the system temperature at the end of the charging and compression processes and the average discharge temperature. It is observed that the highest discharge temperatures occur at the lowest rotational speed (Cases 1–3). This value decreases as the duration of the compression process decreases (i.e., at higher rotational speed). Also, the higher inlet velocity proportionally increases the temperature build up during the cycle. The maximum average temperature difference between the inlet and outlet flow (ΔT) is 17 K, while the lowest is 1 K. These values are not drastically high compared to the conventional compression processes. However, the effect of the temperature increase on the trans-critical CO_2 refrigeration cycle is subject to its operating conditions and requires a separate analysis.

Table 3. System Internal Temperature (K).

Process	T_1^{max}	T_2^{max}	$\overline{T_{out}}$	ΔT
Case 1	291	296	295	5
Case 2	292	299	297	7
Case 3	295	310	307	17
Case 4	291	293	293	3
Case 5	291	295	294	4
Case 6	292	304	302	12
Case 7	290	292	291	1
Case 8	291	292	292	2
Case 9	292	296	295	5

The compression cycle is initially intended to recover energy from the high-pressure flow by the low-pressure flow. This form of energy transfer needs to be assessed based on the actual transferred energy versus the maximum transferable energy. The effectiveness of the energy transfer process can be quantified by calculating the ratio between the amount of transferred energy to the maximum transferrable energy. In this system, we can use the pressure to calculate the effectiveness. Equation (9) describes the effectiveness as the ratio of the difference between the average discharge and maximum internal pressures at the end of filling process and the internal pressure difference between the end of the compression and filling processes.

$$Effectiveness = \frac{\overline{P_{out}} - P_1^{max}}{P_2^{max} - P_1^{max}} \quad (9)$$

The cycle effectiveness is plotted in Figure 7. The first observation is that all the effectiveness values are positive, which indicates energy transfer between the two flows. The maximum effectiveness of 42.8% is achieved for the lowest rotational speed and highest inlet flow rate (Case 3), while the lowest positive effectiveness is 25.7% for Case 1. The inlet velocity/flow rate positively affects the system's effectiveness at a given rotational speed. Similarly, the temperature difference monotonically follows the effectiveness trend. This is due to the direct proportionality between the temperature and pressure increase inside the constant volume system. Another observation is the comparable value of effectiveness at a given flow rate for the highest rotational speeds (Cases 4 and 7, Cases 5 and 8, Cases 6 and 9). This is due to the longer process time associated with lower rotational speed. The compression process duration is directly proportional to the pressure ratio.

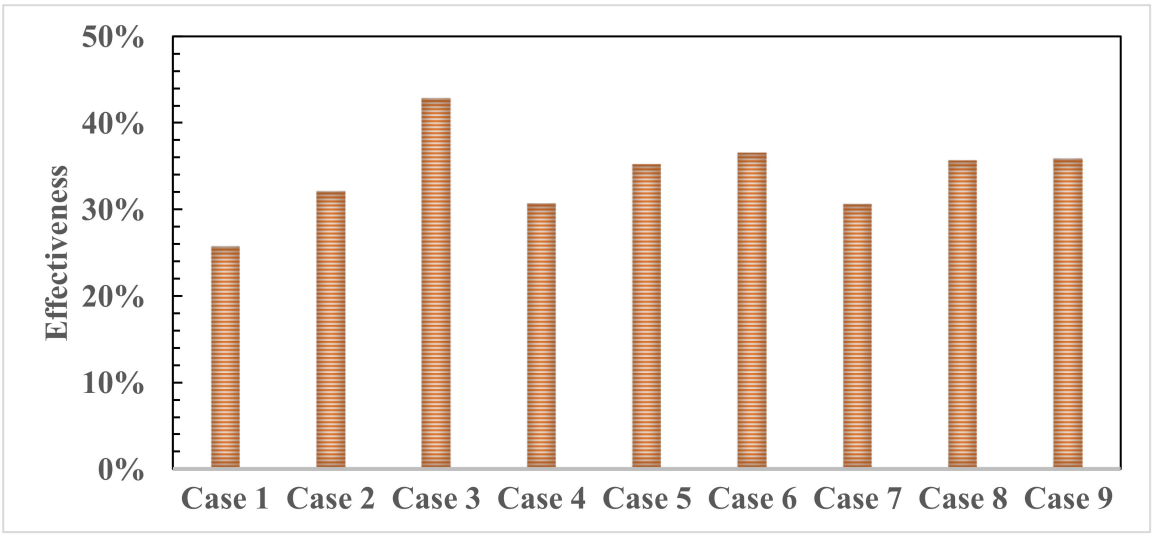

Figure 7. Compression effectiveness and temperature increase.

To have a more clear understanding of how the energy recovery cycle can enhance the performance of trans-critical CO_2 refrigeration cycle, the mixture outlet state for all cases is plotted on the temperature-entropy (*T*-*S*) diagram for CO_2 and presented in Figure 8. The low- and high-pressure flows used in this study are marked on the chart. The low-pressure flow represents the flow condition at the compressor suction side and the high-pressure flow represents the flow at the gas cooler exit. The outlet flow state is found to be located in the superheated flow region for all cases except for Case 3 where the flow is in the supercritical region. As seen in the figure, the outlet flow from the exchange process has gained pressure except for Cases 7 and 8 due to the short process time and the high flow rate. The exchange process is able to generate a single-phase flow which can be directed to the compressor without the need for a separation stage. One can see that the exchange process is customizable to reach the desired flow conditions by controlling the flow rates and rotational speed.

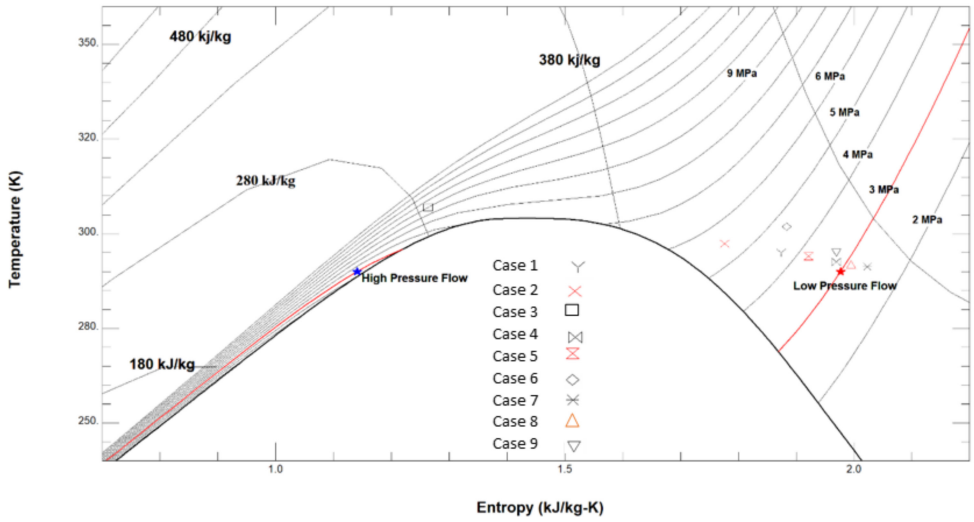

Figure 8. Location of outlet flow state on the temperature-entropy (*T*-*S*) diagram.

For the sake of examining the system characteristics from a different perspective, the exergy (EX) is calculated for the inlet and outlet flows. Since the system is assumed to be adiabatic, the exergy losses due to heat transfer is neglected. Exergy efficiency is the ratio between the system generated exergy and input exergy and calculated as shown in the following equation:

$$\mu_{ex} = \frac{EX_{out}}{EX_P + EX_S} = \frac{\dot{m}_{out}(h_{out} - T_\circ S_{out})}{\dot{m}_p(h_p - T_\circ S_p) + \dot{m}_S(h_S - T_\circ S_S)} \quad (10)$$

where is the reference temperature, h is enthalpy, S is entropy, and is the mass flow rate. The exergetic efficiency is calculated and displayed in Figure 9. It is noted that the exergetic efficiency decreases with the increase of flow rate (i.e., Cases 1–3 and Cases 4–6). This indicates an increase in the exergetic losses. However, this trend is not consistent at the highest rotational speed (Cases 7–9). A plausible explanation for this behavior is that, at the highest system rotational speed, the losses imposed by the system rotation are much higher than the losses caused by the inlet and outlet flow. Therefore, the exergetic efficiency is comparable for Cases 7, 8, and 9, whereas for the lower system rotational speeds, the generated losses due to the flow are relatively more pronounced.

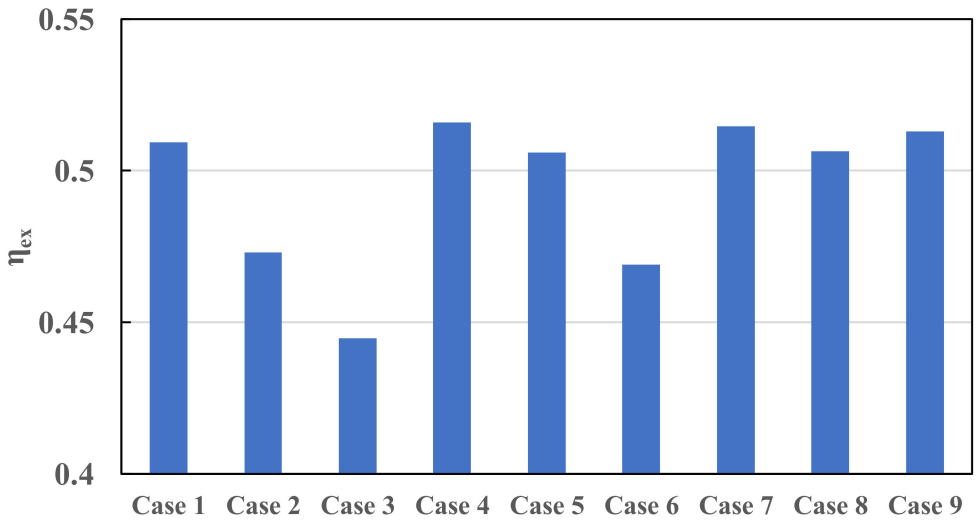

Figure 9. Exergy Efficiency.

4. Discussion

The preliminary thermodynamic analysis of the pressure exchanger system affirms the concept and shows the characteristic prototype behavior with the variation of cycle time and system flow rate. The monotonic behavior of the system properties is clearly seen for most of the tested parameters and is clearly seen in the system pressure and temperature behavior. The simulations show occasionally a temperature build up at certain boundary conditions which reflects the importance of optimizing the system operating conditions to maintain stable conditions. The system effectiveness can be considered as an indicator of the system efficiency based on the system internal pressure only without considering the system mass flow rate effect. The results show an improvement with the increase of flow rate. On the other side, the exergetic efficiency is showing a opposite behavior which can be linked to the incorporation of the mass flow rates of each process in calculating the exergetic efficiency. This behavior shows that the system mass flow rate is negatively affecting the exergetic efficiency and increasing exergy losses.

Another important parameter which plays a key role in the feasibility of implementing a PX in a refrigeration cycle is the energy required to rotate the rotor at the desired speed. While we have not addressed this issue in this proof-of-concept study, we will include this parameter in any future investigation of the actual prototype. Nevertheless, current pressure exchangers used in RO systems may or may not be driven by an electric motor since the rotor channels are hydrodynamically designed to be self-driven by utilizing the kinetic energy of the inlet flows. In other words, the concept of fluid–structure interaction is implemented to transfer part of the flow energy into the rotor body. To achieve proper refrigerant conditions based on refrigeration system operating conditions, implementation of a PX may require the use of an electric motor to control rotational speed. It is expected that the required rotational power will be significantly lower than that recovered by the device as well as that required by the refrigeration system compressors, resulting in an overall increase in system efficiency.

5. Conclusions

A CFD model of a pressure exchange device was generated to investigate the concept of recovering momentum energy for carbon dioxide inside a trans-critical refrigeration cycle. The CFD model was first validated with available published experimental data. This numerical study focused on investigating the effect of the flow rate and process time on the overall behavior of the pressure exchanger system. For simplicity, flow rates for both primary and secondary flows are similar, and the system is considered adiabatic. The effect of speed of rotation was examined by evaluating three rotational speeds. It was found that for the nine cases considered in the study, the recovery process using the proposed system is viable, and the outlet flow can be directed to the compressors of a VC cycle. The overall effectiveness of the pressure exchange device varies from one case to another for the evaluated parameters. The highest effectiveness of 42.8% can be achieved at the longest process time (i.e., lowest rotational speed) and highest flow rate, whereas the cycle effectiveness is lowest for the shortest process time (i.e., highest rotational speed) and lowest flow rate evaluated. The temperature increase through the pressure exchange system ranged from 1 K to 17 K and is directly proportional to the flow rate. In conclusion, the concept of exchanging momentum energy between low- and high-pressure flows in a trans-critical CO_2 refrigeration cycle using the proposed pressure exchange system can increase the cycle performance. This study is an essential step for building and testing a prototype.

Author Contributions: Conceptualization, A.E., B.F., V.S. and K.N.; methodology, A.E., B.F. and V.S.; software, A.E.; validation, A.E.; formal analysis, A.E.; investigation, A.E.; resources, A.E., B.F., V.S. and K.N.; data curation, A.E.; writing—original draft preparation, A.E.; writing—review and editing, A.E., B.F., V.S. and K.N.; visualization, A.E.; supervision, B.F. and K.N.; project administration, B.F. and K.N.; funding acquisition, B.F. All authors have read and agreed to the published version of the manuscript.

Funding: This research was funded by DOE Building Technology Office, USA.

Institutional Review Board Statement: Not applicable.

Informed Consent Statement: Not applicable.

Data Availability Statement: The data can be provided by the corresponding author if requested. This manuscript has been authored by UT-Battelle, LLC, under Contract No. DE-AC05-00OR22725 with the U.S. Department of Energy. The United States Government retains and the publisher, by accepting the article for publication, acknowledges that the United States Government retains a non-exclusive, paid-up, irrevocable, world-wide license to publish or reproduce the published form of this manu-script, or allow others to do so, for United States Government purposes.

Acknowledgments: The authors acknowledge the support provided by DOE Building Technologies Office and the Technology Manager, Antonio Bouza.

Conflicts of Interest: The authors declare no conflict of interest.

References

1. Sharma, V.; Fricke, B.; Bansal, P. Evaluation of a trans-critical CO_2 supermarket refrigeration system for the USA market. In Proceedings of the 6th Ammonia and CO_2 Refrigeration Technology Conference, Ohrid, North Macedonia, 16–18 April 2015.
2. Fricke, B.; Zha, S.; Sharma, V.; Newel, J. Laboratory evaluation of a commercial CO_2 booster refrigeration system. In Proceedings of the 16th International Refrigeration and Air Conditioning Conference at Purdue, Purdue, IN, USA, 11–14 July 2016.
3. Gullo, P. Innovative fully integrated trans-critical R744 refrigeration systems for a HFC-free future of supermarkets in warm and hot climates. *Int. J. Ref.* **2019**, *108*, 283–310. [CrossRef]
4. Groll, E.; Kim, J.H. Review article: Review of recent advances toward trans-critical CO_2 cycle technology. *HVAC&R Res.* **2007**, *13*, 499–520.
5. Nakagawa, M.; Berana, M.S.; Kishinec, A. Supersonic two-phase flow of CO_2 through converging-diverging nozzles for the ejector refrigeration cycle. *Int. J. Ref.* **2009**, *32*, 1195–1202. [CrossRef]
6. Nakagawa, M.; Marasigan, A.R.; Matsukawa, T.; Kurashina, A. Experimental investigation on the effect of mixing length on the performance of two-phase ejector for CO_2 refrigeration cycle with and without heat exchanger. *Int. J. Refrig.* **2011**, *34*, 1604–1613. [CrossRef]
7. Elbel, S.; Hrnjak, P. Experimental validation of a prototype ejector designed to reduce throttling losses encountered in transcritical R744 system operation. *Int. J. Refrig.* **2008**, *31*, 411–422. [CrossRef]
8. Bartosiewicz, Y.; Aidoun, Z.; Mercadier, Y. Numerical assessment of ejector operation for refrigeration applications based on CFD. *Appl. Therm. Eng.* **2006**, *26*, 604–612. [CrossRef]
9. Banasiak, K.; Hafner, A. 1D Computational model of a two-phase R744 ejector for expansion work recovery. *Int. J. Therm. Sci.* **2011**, *50*, 2235–2247. [CrossRef]
10. Besagni, G.; Mereu, R.; Inzoli, F. Ejector refrigeration: A comprehensive review. *Renew. Sustain. Energy Rev.* **2016**, *53*, 373–407. [CrossRef]
11. He, Y.; Deng, J.; Zhang, L.; Zhang, Z. Performance optimization of a trans-critical CO_2 refrigeration system using a controlled ejector. *Int. J. Refrig.* **2017**, *75*, 250–261. [CrossRef]
12. Carrillo, J.A.E.; La Flor, F.J.S.; Lissen, J.M.S. Single-phase ejector geometry optimization by means of a multi-objective evolutionary algorithm and a surrogate CFD model. *Energy* **2018**, *164*, 46–64. [CrossRef]
13. Carrillo, J.A.E.; La Flor, F.J.S.; Perís-Perez, B.; Lissen, J.M.S. Thermodynamic analysis of the optimal operating conditions for a two-stage CO_2 refrigeration unit in warm climates with and without ejector. *Appl. Therm. Eng.* **2021**, *185*, 116284. [CrossRef]
14. Qi, B.; Wang, Y.; Wang, Z.; Zhang, Y.; Xu, S.; Wang, S. Theoretical investigation on internal leakage and its effect on the efficiency of fluid switcher-energy recovery device for reverse osmosis desalting plant. *Chin. J. Chem. Eng.* **2013**, *21*, 1216–1223. [CrossRef]
15. Wang, Z.; Wang, Y.; Zhang, Y.; Qi, B.; Xu, S.; Wang, S. Pilot tests of fluid-switcher energy recovery device for seawater reverse osmosis desalination system. *Desalin. Water Treat.* **2012**, *48*, 310–314. [CrossRef]
16. Gude, V.G. Energy consumption and recovery in reverse osmosis. *Desalin. Water Treat.* **2011**, *36*, 239–260. [CrossRef]
17. Stover, R.L. Development of a fourth-generation energy recovery device. A'CTO's Notebook'. *Desalination* **2004**, *165*, 313–321. [CrossRef]
18. Lemmon, E.W.; Huber, M.L.; McLinden, M.O. *NIST Reference Fluid Thermodynamic and Transport Properties—REFPROP, Version 9.1.*; National Institute of Standards and Technology: Gaithersburg, MD, USA, 2013.
19. Xu, E.; Wang, Y.; Wu, L.; Xu, S.; Wang, Y.; Wang, S. Computational fluid dynamics simulation of brine-seawater mixing in a rotary energy recovery device. *Ind. Eng. Chem. Res.* **2014**, *53*, 18304–18310. [CrossRef]